Reconstruction of MR Images from Data Acquired on a General Nonregular Grid by Pseudoinverse Calculation

Rik Van de Walle*, Harrison H. Barrett, Kyle J. Myers, Maria I. Altbach, Bart Desplanques, Arthur F. Gmitro, Jan Cornelis, and Ignace Lemahieu

***Abstract*—A minimum-norm least-squares image-reconstruction method for the reconstruction of magnetic resonance images from non-Cartesian sampled data is proposed. The method is based on a general formalism for continuous-to-discrete mapping and pseudoinverse calculation. It does not involve any regridding or interpolation of the data and therefore the methodology differs fundamentally from existing regridding-based methods. Moreover, the method uses a continuous representation of objects in the image domain instead of a discretized representation. Simulations and experiments show the possibilities of the method in both radial and spiral imaging. Simulations revealed that minimum-norm least-squares image reconstruction can result in a drastic decrease of artifacts compared with regridding-based reconstruction. Besides, both *in vivo* and phantom experiments showed that minimum-norm least-squares image reconstruction leads to contrast improvement and increased signal-to-noise ratio compared with image reconstruction based on regridding. As an appendix, an analytical calculation of the raw data corresponding to the well-known Shepp and Logan software head phantom is presented.**

***Index Terms*—Generalized reconstruction, magnetic resonance imaging, medical imaging, pseudoinverse image reconstruction.**

I. Introduction

FOR MANY years, two-dimensional (2-D) Fourier transform (2DFT) imaging has been the most popular method in magnetic resonance imaging (MRI), in which the MR signals are sampled on a rectilinear or Cartesian grid in the spatial-frequency k-space. The very efficient fast Fourier transform (FFT) [1], [2] can then be applied to transform the spatial-frequency components into the desired image-domain intensities, which keeps reconstruction times short.

At present, non-Cartesian sampling schemes are becoming more popular in MRI. For example, extensive research on radial sampling has been performed and it has in particular been shown that radial sampling is less sensitive to motion than standard 2DFT imaging [3]–[11]. Several clinical applications of MRI (e.g., functional MRI and dynamic contrast-agent imaging) rely on fast data-acquisition schemes that utilize non-Cartesian sampling grids, including some forms of echo-planar imaging [12], spiral imaging [13]–[16], rosette trajectories [17], [18], and the application of stochastic k-space trajectories [19].

In the case of radial sampling, the filtered backprojection (FBP) algorithm can be used for the image reconstruction [20]–[22]. Another method that is widely used to reconstruct images from data that are sampled on a non-Cartesian grid, especially in spiral imaging, is the so-called regridding method [23]–[25]. In this method, the nonrectilinearly measured data points are resampled onto a Cartesian grid by using an appropriate convolution kernel and then the FFT algorithm is used to reconstruct the images. Other techniques, allowing the use of the FFT algorithm in the case of non-Cartesian data acquisition, have been developed as well: e.g., Axel *et al.* proposed the so-called linogram reconstruction for MRI, an alternative to conventional convolution/backprojection methods of reconstruction from projections [26]. A major advantage of this method is the fact that it avoids the computationally intensive interpolations required for backprojection. As a result, linograms offer significant savings in reconstruction time over conventional backprojection.

In this paper, we propose an alternative for the reconstruction of MR images from a nonuniform data grid without using any regridding or interpolation of the acquired data. The method is based on the fact that MR data acquisition is a special case of a continuous-to-discrete (CD) mapping, i.e., a mapping of the continuous object space into a discrete and finite set of data samples in k-space. The reconstruction of an image from the measured data can then be seen as finding an inverse for this mapping. In practice, the exact inverse mapping does not exist and therefore an exact reconstruction of the original object function cannot be obtained. In this paper, we introduce a method for the calculation of the minimum-norm least-squares solution of the inverse mapping problem.

In the following section, the theory that forms the basis for the image-reconstruction method is explained in general and specif-

Manuscript received November 24, 1999; revised September 22, 2000. This work was supported by the Fund for Scientific Research, Flanders (FWO, Belgium), the Flemish Institute for the Promotion of Scientific-Technological Research in the Industry (IWT, Belgium), the NCI (USA) under Grant CA52643B, and the National Institutes of Health (NIH) under Grant HL03528. The Associate Editor responsible for coordinating the review of this paper and recommending its publication was V.Johnson. *Asterisk indicates corresponding author.*

*R. Van de Walle, B. Desplanques, and I. Lemahieu are with the Department of Electronics and Information Systems, Ghent University, Ghent, B-9000 Belgium (e-mail: rik.vandewalle@rug.ac.be).

H. H. Barrett, and A. F. Gmitro are with the Department of Radiology, and are also with the Optical Sciences Center, University of Arizona, Tucson, AZ, USA.

M. I. Altbach is with the Department of Radiology, University of Arizona, Tucson, AZ, USA.

K. J. Myers is with the Center for Devices and Radiological Health, Food and Drug Administration, USA.

J. Cornelis is with the Department of Electronics and Information Processing, Free University of Brussels, Brussels, Belgium.

Publisher Item Identifier S 0278-0062(00)10881-X.

ically for the case of MRI. The theory developed here is related to the theory proposed in [27], [28]. Its use in the case of reconstruction based on the radon transform was already described in the past [29]–[31]. In this paper, however, it is shown that this theory can be used not only for backprojection-based reconstruction methods but also for a wide variety of MRI reconstruction problems (e.g., for the reconstruction of images from data sampled on a spiral trajectory).

By performing simulations and MR experiments the method is compared with existing reconstruction methods. In the simulations, the Shepp and Logan software head phantom is considered [32]. Therefore, an analytical expression for the raw data that correspond to this phantom was calculated. A summary of these calculations is added to this paper as an appendix.

It should be noticed that this paper describes a reconstruction method yielding a *continuous* reconstruction of the image function in the case of MRI, which, as far as we know, has not been reported previously. For example, in [33] the continuous description of MRI data acquisition is discretized prior to the image reconstruction based on a linear algebraic model. In this paper, it will be shown that this discretization step is not necessary in order to be able to reconstruct the images.

II. Theory

During an MR experiment, M data points are acquired in the spatial-frequency domain. The mth data point g_m is equal to the spatial-frequency component at the spatial frequency $\overline{k}_m$ and can therefore be written as

$$g_m = \int_D d\overline{r}\, I(\overline{r}) \exp\left(-j2\pi \overline{k}_m \cdot \overline{r}\right) \tag{1}$$

where

- $\overline{r}$ position vector;
- $I(\overline{r})$ image function to be depicted (i.e., the complex transverse-magnetization distribution);
- D is the field of view (FOV).

The purpose of image reconstruction is to find an estimate of the exact image $I(\overline{r})$ given the data set $\{g_m;\ m = 1, \ldots, M\}$. Note that in all practical situations the image function $I(\overline{r})$ is a continuous function of the position vector $\overline{r}$, while the data are collected on a discrete and finite grid. In other words, data acquisition in MRI corresponds to a linear CD mapping on a finite grid, and it is, therefore, not possible to calculate the exact value of the image function for all values of $\overline{r}$ in D. As a result, the image-reconstruction problem is equivalent to finding "a good estimate" $\hat{I}(\overline{r})$ of $I(\overline{r})$.

In the remaining part of this section, we describe how the minimum-norm least-squares (MNLS) estimate $\hat{I}_{\mathrm{MNLS}}(\overline{r})$ of $I(\overline{r})$ can be calculated. Therefore, we need to introduce the notions adjoint and pseudoinverse of a linear operator. The mathematical description for a general CD mapping will be proposed first, followed by a description specific to the case of MRI.

A. General CD mapping

Consider the general linear CD mapping of a continuous function $f(\overline{r})$ to a discrete and finite set of data points $\{g_m;\ m = 1, \cdots, M\}$. Mathematically, such a mapping can be described by

$$g_m = \int_D d\overline{r}\, f(\overline{r})\, h_m(\overline{r}) \tag{2}$$

where $h_m(\overline{r})$ is the so-called point-response function of the CD mapping. This CD mapping can be described by an operator equation as well

$$\mathbf{g} = \mathcal{H} f(\overline{r}). \tag{3}$$

The operator $\mathcal{H}$ maps a linear vector space U in to a linear vector space V, with $f(\overline{r}) \in U$ and $\mathbf{g} \in V$. In this paper, we will assume that $\mathcal{H}$ is a compact operator. Moreover, we will assume $U = L_2(D)$, i.e, U is the space of square-integrable functions over D. The set of data points will be described by acomplex column vector $\mathbf{g}$ and therefore the space V is chosen to be $\mathbf{C}^{M\times 1}$. Both U and V are Hilbert spaces in which scalar products can be defined as discussed in [34].

Once a CD operator $\mathcal{H}$ that maps a Hilbert space U into a Hilbert space V is defined, its adjoint operator $\mathcal{H}^\dagger$ that maps V into U [and which is, therefore, a discrete-to-continuous (DC) operator] can be defined by [35]

$$\left[\mathcal{H}^\dagger \mathbf{g}\right](\overline{r}) = \sum_{m=1}^{M} g_m\, h_m^*(\overline{r}). \tag{4}$$

As stated earlier, the general reconstruction problem that is dealt with in this paper is calculating an estimate $\hat{f}(\overline{r})$ for $f(\overline{r})$ when $\mathbf{g} = \mathcal{H} f(\overline{r})$ is given. Here, we will try to find the MNLS solution of equation (3). The notion of the (Moore–Penrose) pseudoinverse allows us to find the MNLS solution $\hat{f}_{\mathrm{MNLS}}(\overline{r})$ of (3) [36], [37]

$$\hat{f}_{\mathrm{MNLS}}(\overline{r}) = \mathcal{H}^+ \mathbf{g} \tag{5}$$

with $^+$ denoting the Moore–Penrose pseudoinverse.

To be able to calculate this MNLS solution it is necessary to calculate the pseudoinverse $\mathcal{H}^+$ of $\mathcal{H}$, and the latter can be performed by using the following equation:

$$\mathcal{H}^+ = \mathcal{H}^\dagger (\mathcal{H}\mathcal{H}^\dagger)^+ \tag{6}$$

Therefore, we need to investigate the operator $\mathcal{H}\mathcal{H}^\dagger$ more closely. The operator $\mathcal{H}\mathcal{H}^\dagger$ is a matrix operator that maps V into itself, and it can therefore be represented by an element of $\mathbf{C}^{M\times M}$. In the remaining part of this paper, we will often shortly refer to this matrix operator as "the matrix" $\mathcal{H}\mathcal{H}^\dagger$. The corresponding matrix elements $\{[\mathcal{H}\mathcal{H}^\dagger]_{mn};\ m, n = 1, \ldots, M\}$ are found to be

$$\left[\mathcal{H}\mathcal{H}^\dagger\right]_{mn} = \int_D d\overline{r}\, h_n^*(\overline{r})\, h_m(\overline{r}). \tag{7}$$

From this equation it is easily seen that $\mathcal{H}\mathcal{H}^\dagger$ is a Hermitian operator.

$(\mathcal{H}\mathcal{H}^\dagger)^+$ can be calculated by performing the singular value decomposition (SVD) of $\mathcal{H}\mathcal{H}^\dagger$. The eigenvalue equation for the operator $\mathcal{H}\mathcal{H}^\dagger$ is given by $\mathcal{H}\mathcal{H}^\dagger \mathbf{v}_k = \lambda_k \mathbf{v}_k$, with $\mathbf{v}_k$ and λ_k the kth eigenvector and eigenvalue, respectively. Operators of the

form $\mathcal{H}\mathcal{H}^\dagger$ have real and nonnegative eigenvalues [35]. Moreover, it is convenient to order the eigenvalues λ_k by increasing value, such that $\lambda_k = 0$ for $k = 1, \cdots, M-R$ and $\lambda_k \neq 0$ for $k = M-R+1, \cdots, M$, with R being the rank of $\mathcal{H}\mathcal{H}^\dagger$. From this, the general MNLS solution of (3) is found to be

$$\hat{f}_{\mathrm{MNLS}}(\overline{r}) = \sum_{m=1}^{M} \left[\left(\sum_{k=M-R+1}^{M} \frac{1}{\lambda_k} \mathbf{v}_k \mathbf{v}_k^\dagger \right) \mathbf{g} \right]_m h_m^*(\overline{r}). \quad (8)$$

B. MRI as a Special Case of CD Mapping

The formalism described above is valid for any CD mapping of U into V that satisfies equation (2). By comparing the latter equation with the MRI equation that is given in equation (1), it is seen that MR data acquisition can be described by a CD mapping of U into V with

$$h_m(\overline{r}) = \exp\left(-j2\pi \overline{k}_m \cdot \overline{r}\right). \quad (9)$$

By substituting equation (9) into equation (7), one finds

$$\left[\mathcal{H}\mathcal{H}^\dagger\right]_{mn} = W(\overline{k}_m - \overline{k}_n), \quad (10)$$

where $W(\overline{k}) = \mathcal{F}\left[w(\overline{r})\right](\overline{k})$, $\mathcal{F}(\cdot)$ denoting the Fourier transform and $w(\overline{r})$ being the support function

$$w(\overline{r}) = \begin{cases} 1, & \text{if } \overline{r} \in D \\ 0, & \text{otherwise.} \end{cases} \quad (11)$$

In other words, in the case of MRI, the matrix element $[\mathcal{H}\mathcal{H}^\dagger]_{mn}$ equals the Fourier transform of the support function evaluated at the spatial frequency $\overline{k}_m - \overline{k}_n$.

In the simulations and experiments that are described below, 2-D MRI with a square FOV of dimension F is considered. Then, the (x, y) plane can be chosen to be the image plane and the support function becomes $w(\overline{r}) = w(x, y)\delta(z)$, where $\delta(.)$ is denoting the delta function and the 2-D in-plane support function $w(x, y)$ is given by

$$w(x, y) = \begin{cases} 1, & \text{if } |x| \leq \dfrac{F}{2} \text{ and } |y| \leq \dfrac{F}{2} \\ 0, & \text{otherwise.} \end{cases} \quad (12)$$

By substituting this support function in equation (10) we find

$$\begin{aligned} \left[\mathcal{H}\mathcal{H}^\dagger\right]_{mn} = {} & F^2 \mathrm{sinc}\left(\pi(k_{mx} - k_{nx})F\right) \\ & \times \mathrm{sinc}\left(\pi(k_{my} - k_{ny})F\right) \end{aligned} \quad (13)$$

with $\overline{k}_m = (k_{mx}, k_{my})$, $\overline{k}_n = (k_{nx}, k_{ny})$, and $\mathrm{sinc}(x) = \sin(x)/x$.

A special case of sampling is standard Cartesian sampling with fulfillment of the Nyquist condition. Then, the former expression reduces to $[\mathcal{H}\mathcal{H}^\dagger]_{mn} = F^2\delta_{mn}$ with δ_{mn} denoting the Kronecker delta. In this particular case the MNLS solution of equation (1) is given by

$$\hat{I}_{\mathrm{MNLS}}(\overline{r}) = \frac{1}{F^2} \sum_{m=1}^{M} g_m \exp\left(j2\pi \overline{k}_m \cdot \overline{r}\right). \quad (14)$$

In other words, in the case of Cartesian sampling with fulfillment of the Nyquist condition, MNLS image reconstruction is equivalent to calculating the inverse discrete Fourier transform of the data matrix.

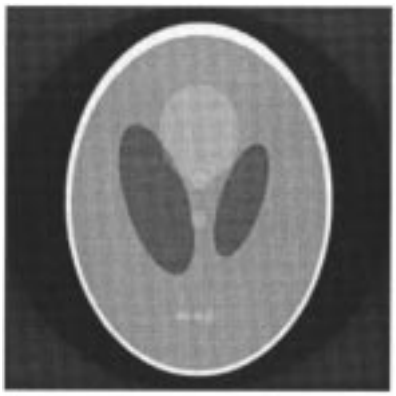

Fig. 1. The Shepp and Logan software head phantom.

In the general case of MRI, however, the MNLS solution should be calculated from (4)–(6), (8), and (9)

$$\begin{aligned} \hat{I}_{\mathrm{MNLS}}(\overline{r}) = {} & \sum_{m=1}^{M} \left[\sum_{k=M-R+1}^{M} \left(\frac{1}{\lambda_k} \mathbf{v}_k \mathbf{v}_k^\dagger \right) \mathbf{g} \right]_m \\ & \times \exp\left(j2\pi \overline{k}_m \cdot \overline{r}\right). \end{aligned} \quad (15)$$

III. Methods

Simulations and in vivo experiments were performed to explore the possibilities of the proposed MNLS image-reconstruction technique. Although this method can be used with any trajectory in k-space, attention was restricted to the cases of radial and spiral MRI in this study. The SVD-based reconstruction technique was implemented on a Compaq Personal Workstation (500 au, 704-Mb RAM). In order to solve the corresponding real symmetric eigenvalue problem, we used routines from the LAPACK/BLAS package (Linear Algebra PACKage; Basic Linear Algebra Subprograms) [38]. More specifically, the Double precision; SYmmetric EigenValue problem (DSYEV) routine was used. The FBP algorithm (cf., infra) was implemented in IDL (Research Systems, Inc.) on a personal computer. The in vivo experiments were performed on a clinical 1.5-T GE (Milwaukee, WI) Signa MR scanner.

In all simulations, the Shepp and Logan (SL) software head phantom was considered [32]. This phantom consists of ten ellipses with different intensities and orientations and is shown in Fig. 1. In this paper, we are treating MR data acquisition as a special case of a CD mapping. Therefore, we used the continuous representation of the SL phantom rather than a discretized representation of it. In appendix it is shown how the raw Fourier data that correspond to an ellipse that is centered at an arbitrary point (x_1, y_1) and rotated by an angle α relative to the x-axis can be calculated analytically. The continuous raw-data function $S_\theta(k)$ as a function of the spatial-frequency variable $\overline{k} = k\exp(j\theta)$ is found to be

$$S_\theta(k) = \exp\left[-j2\pi kt\cos(\gamma - \theta)\right] \rho AB \frac{J_1(2\pi a(\theta)k)}{a(\theta)k} \quad (16)$$

where

t $= \sqrt{x_1^2 + y_1^2}$;
γ $= \arctan(y_1/x_1)$;
$a(\theta)$ $= \sqrt{A^2\cos^2(\theta-\alpha) + B^2\sin^2(\theta-\alpha)}$;
A, B short and long axes of the ellipse;
ρ intensity of the ellipse;
$J_1(\cdot)$ denotes the first-order Bessel function of the first kind.

Note that equation (16) gives the raw data of the general ellipse in polar (k, θ)-coordinates in k-space. The continuous raw-data function $S_{\mathrm{SL},\theta}(k)$ of the SL phantom was calculated from equation (16) by adding the raw-data functions that correspond to each of the ten ellipses in the phantom.

A. Radial Imaging

As a first application of the theoretical concept that was described above, simulations were performed with N_θ =64 uniformly distributed radial lines in k-space and N_r =64 uniformly distributed data points along each radial line. The radial and azimuthal sample spacings were $\Delta r = (1/F)$ and $\Delta\theta = (\pi/N_\theta)$, with F being the size of the square FOV. From these, the set of spatial frequencies $\{\overline{k}_m;\ m = 1, \ldots, M\}$ was calculated. In the simulations, the elements of the raw-data matrix $\mathbf{g}$ were calculated by $g_m = S_{\mathrm{SL},\theta_m}(k_m)$ for $m = 1, \ldots, M$. Although in standard radial scanning the data point at the origin of the k-space is acquired for each radial line, this central data point was counted only once during the MNLS image reconstruction. Therefore, only $M = N_r + (N_r - 1)(N_\theta - 1) = 4033$ different data points were used in the calculations instead of $N_r N_\theta$.

According to equation (13), the matrix elements $[\mathcal{H}\mathcal{H}^\dagger]_{mn}$ were calculated for each $m, n = 1, \ldots, M$. The solution of the eigenvalue problem corresponding to the matrix $\mathcal{H}\mathcal{H}^\dagger$ was found as described before. Next, the radial MNLS image function $\hat{I}_{\mathrm{MNLS}}(\overline{r})$ was calculated by applying (15). In order to be able to visualize the image function, it was discretized on a Cartesian grid in the image domain. It should be emphasized, however, that discretization in the image domain is performed only at this occasion, i.e., after the actual image reconstruction and as a sampling of a continuous image reconstruction.

The radial MNLS images were compared with the images obtained when zero-padded FBP is applied on the same raw-data matrix. In our implementation of the FBP algorithm, the standard approach that was proposed in [10], [22], and [39] was followed.

B. Spiral Imaging

Both simulated imaging of the SL head phantom and transverse human head imaging with F =240 mm were performed with spiral data acquisition. In the in vivo experiments, the echo time was set to 40 ms in a first experiment and to 60 ms in a second experiment in order to increase the T_2 contrast, and the slice thickness was 5 mm. A one-interleave spiral was used throughout this study, which contained M =3520 different data points. The corresponding trajectory in k-space is shown in Fig. 2. In the simulations, the raw-data matrix $\mathbf{g}$ was again calculated from the knowledge of the k-space trajectory and $S_{\mathrm{SL},\theta}(k)$. The matrix elements $[\mathcal{H}\mathcal{H}^\dagger]_{mn}$ were calculated for each $m, n = 1, \ldots, M$. The SVD calculation of the matrix $\mathcal{H}\mathcal{H}^\dagger$ and the

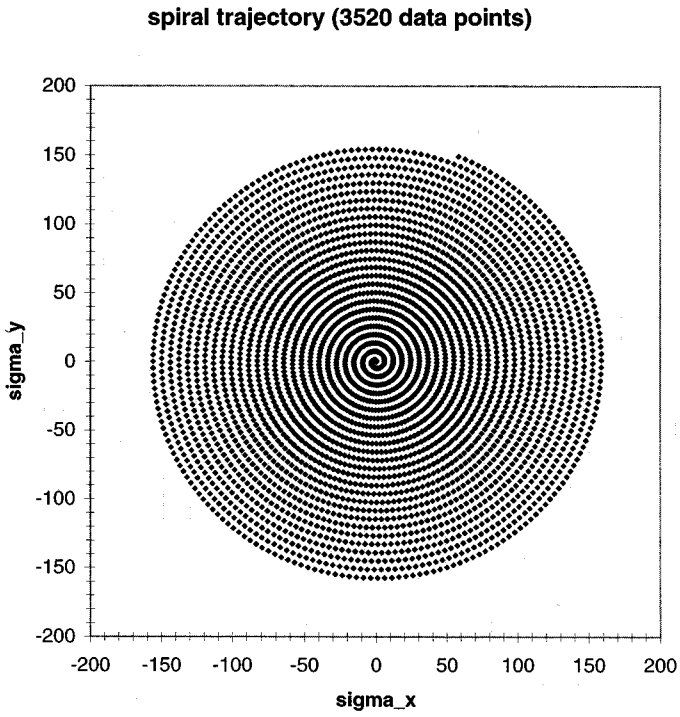

Fig. 2. Trajectory in k-space in the case of one-interleave spiral imaging with 3520 data points.

calculation of the MNLS image functions were performed analogously to the algorithm that was described for radial imaging.

The spiral MNLS images were compared with the images obtained using the regridding method that is described in [24], which is very widely used in practice because it is computationally fast and robust to measurement errors [40]. The raw data were first regridded onto a rectilinear grid by using a discrete Kaiser–Bessel window

$$w(n) = \begin{cases} \dfrac{I_0\left(B\sqrt{1-\left(\dfrac{2n}{N-1}\right)^2}\right)}{I_0(B)}, & \text{if } -\dfrac{N-1}{2} \le n \le \dfrac{N-1}{2} \\ 0, & \text{otherwise} \end{cases} \tag{17}$$

where $I_0(\cdot)$ is the zeroth-order modified Bessel function of the first kind. We used a width of N =4 and a B-value of eight. Following the regridding, the FFT algorithm was applied to reconstruct the images.

IV. Results and Discussion

We will first discuss the results for the case of radial imaging. The eigenvalues, λ_k, obtained from solving the eigenvalue problem corresponding to $\mathcal{H}\mathcal{H}^\dagger$, are shown in Fig. 3 for the case of $N_\theta = N_r = 64$. Until now we assumed that the matrix $\mathcal{H}\mathcal{H}^\dagger$ is either singular or not. A singular matrix corresponds to one for which some of the eigenvalues are identically equal to zero. Although it is difficult to appreciate in Fig. 3, some of the λ_k are very small but none are numerically equal to zero. As a result, although nonsingular, the corresponding $\mathcal{H}\mathcal{H}^\dagger$ matrix

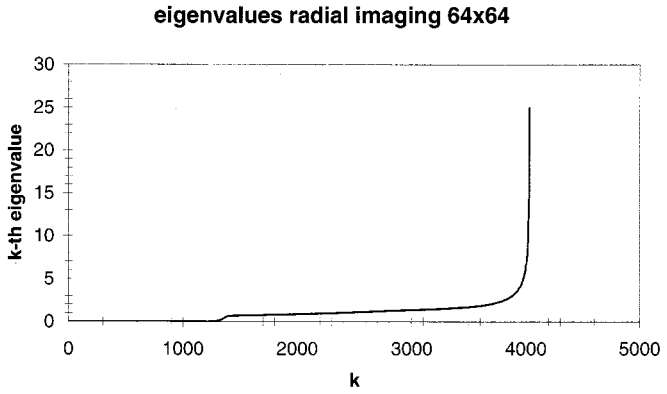

Fig. 3. Singular values in the case of 64×64 radial imaging.

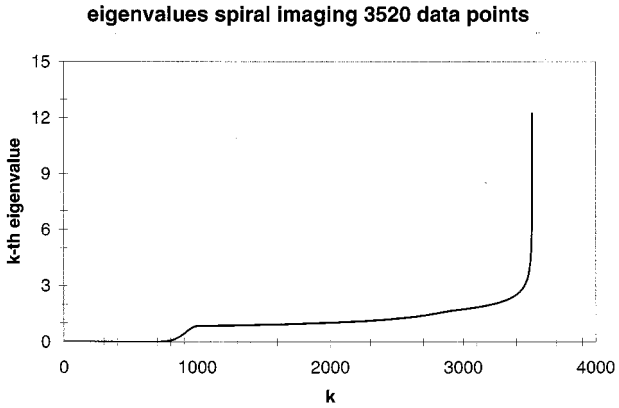

Fig. 5. Singular values in the case of spiral imaging with 3520 data points.

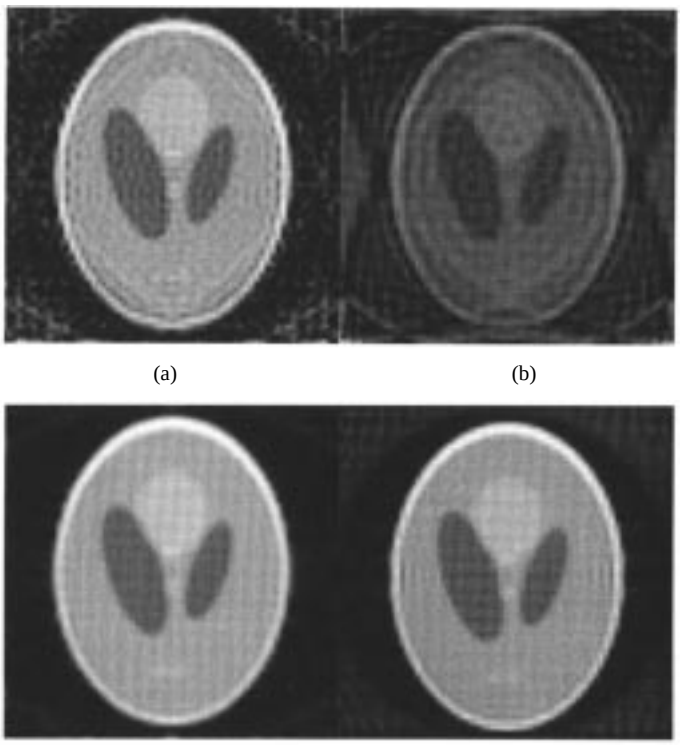

(a) (b)

(c) (d)

Fig. 4. The influence of the value of the threshold T on the corresponding MNLS image. (a) MNLS image reconstructed without threshold (i.e., $T = 0$). It contains severe artifacts due to roundoff errors. (b) Reconstructed with a threshold of $T = 1.0$ and contains severe artifacts due to the fact that too many terms are zeroed. (c) MNLS image that is reconstructed with a threshold $T_{64\times64}$ =0.65. (d) Shows the image that is obtained after FBP. The image quality for MNLS image reconstruction with a suitable threshold and FBP is comparable.

is ill-conditioned, and this can cause serious roundoff errors during the SVD calculation [1]. The illconditionedness of $\mathcal{H}\mathcal{H}^{\dagger}$ can be expressed by calculating its so-called condition number, i.e., the ratio of its largest and its smallest singular value. The higher this condition number the more the corresponding matrix is ill-conditioned. For the simulations that are discussed here, the condition number was $1.6e+11$.

Direct application of equation (15) would lead to the assumption $R = M$ since numerically none of the λ_k are zero. However, in situations where the condition number is large, it is often useful to use a threshold T for the calculation of $1/\lambda_k$: $1/\lambda_k$ is set to 0 when $\lambda_k < T$. In Fig. 4, the importance of choosing a suitable threshold T is illustrated for the case of 64×64 radial imaging. Fig. 4(a) is reconstructed without threshold and contains severe artifacts due to numerical errors that are accumulated during the SVD calculation. Fig. 4(b) is reconstructed with a threshold of T =1.0 and contains severe artifacts as well. This is due to the fact that too many terms are zeroed in (15) when T =1.0 is used (cf., Fig. 3). A suitable threshold can be chosen by looking at the behavior of the eigenvalues in Fig. 3. A threshold was chosen near the "kink" where the λ_k start to drop to very small values. With a threshold of $T_{64\times64}$ =0.65, the image shown as Fig. 4(c) in Fig. 4 is obtained. Fif. 4(d) shows the image obtained with standard FBP. The image quality for MNLS image reconstruction with a suitable threshold and FBP is comparable, although the MNLS image contains slightly less severe ringing artifacts.

As is stated in [31], the use of a threshold for the calculation of $1/\lambda_k$ regularizes the resulting images. This is a special case of a more general approach, in which one tries to minimize the large noise amplification that is often observed when pseudoinverse calculations are performed in a straightforward way (i.e., without regularization). Other solutions for the ill-posedness and (numerical) accuracy problems encountered when pseudoinverse calculations are performed have been reported already, including the method of Tikhonov–Phillips, the use of iterative reconstruction methods, or methods based on statistics [41], [31]. The use of these methods implies some smoothness requirement. Fig. 4 can be considered to be an illustration of this.

The λ_k values for the case of spiral imaging with 3520 data points are shown in Fig. 5. A threshold T_{3520} =0.85 was derived from this plot. In Fig. 6 the corresponding MNLS image of the SL phantom is compared with the image obtained with regridding and FFT. The MNLS image contains obviously less artifacts than the image obtained with the regridding algorithm. This is also seen in Fig. 7. In this figure, the pixel intensities along a horizontal line at the center of the FOV are compared

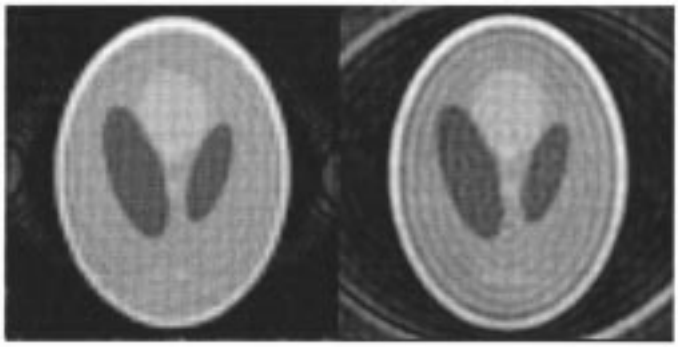

(a) (b)

Fig. 6. (a) Comparison of the MNLS and (b) regridding-based simulated SL phantom reconstruction in the case of spiral imaging with 3520 data points.

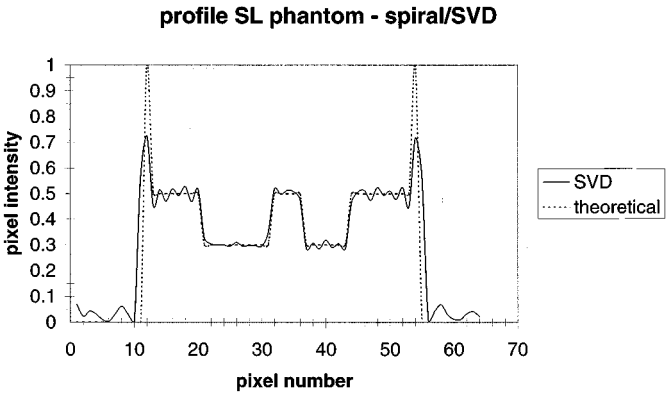

(a)

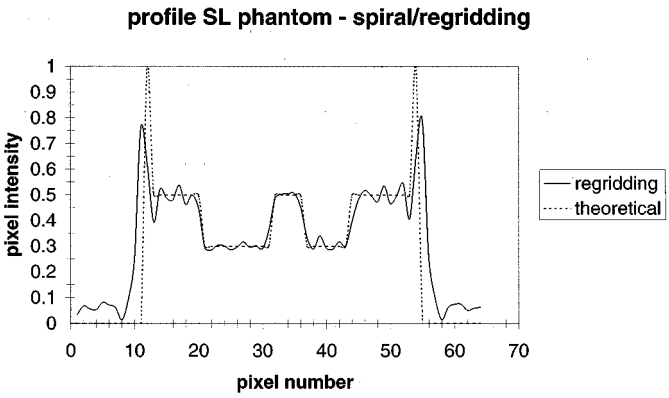

(b)

Fig. 7. Pixel intensities along a horizontal line at the center of the FOV, compared with the theoretical pixel intensities in (a) the MNLS and (b) regridding images that are shown in Fig. 6. The ringing artifacts and overshoot at edges are more pronounced in the case of regridding-based image reconstruction than in the case of MNLS image reconstruction.

with the theoretical pixel intensities for both images. The amplitude of the ringing artifacts and the overshoot at edges are more pronounced in the case of regridding-based image reconstruction than in the case of MNLS image reconstruction.

Fig. 8 shows transverse images of a human head obtained with the one-interleave spiral trajectory containing 3520 different data points. Again, the MNLS images contain

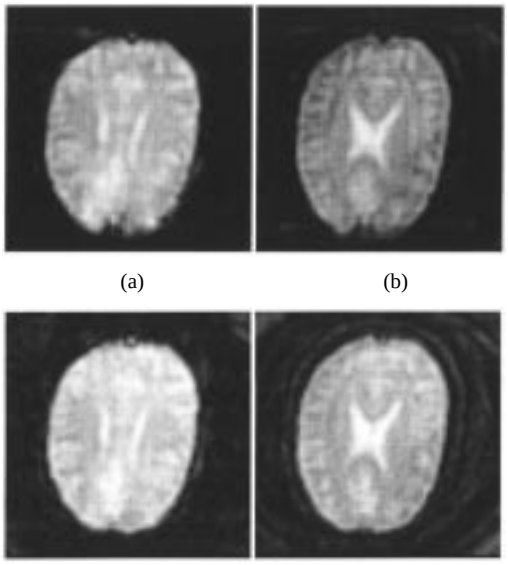

(a) (b)

(c) (d)

Fig. 8. Transverse images of a human head reconstructed from 3520 data points along a one-interleave spiral trajectory. (a) MNLS image with TE $= 40$ ms. (b) Corresponding image obtained after regridding and FFT. (c) MNLS image with TE $= 60$ ms. (d) Corresponding image obtained after regridding and FFT. As in the simulations, the MNLS images contain less artifacts. Moreover, the image contrast and SNR are superior in the MNLS images.

significantly less artifacts than the images obtained from regridding-based image reconstruction. Moreover, the contrast in the MNLS images is higher than the contrast in the corresponding regridding-based images. Finally, from the observation of the images in Fig. 8, the signal-to-noise ratio (SNR) of the MNLS images seems to be higher than the SNR of the images that are reconstructed after regridding of the data. In order to quantify this SNR increase, imaging of a uniform water phantom was performed, by using the same spiral trajectory that was used for the *in vivo* experiments. Two images of the same phantom were acquired and from these, a difference image was calculated. The SNR of the phantom images was calculated by dividing the mean pixel intensity in the phantom by the standard deviation of the pixel distribution in the difference image. This resulted in a SNR of 30 in the case of regridding-based reconstruction and a SNR of 36 in the case of MNLS image reconstruction.

Recently, a study on the optimality of the regridding method has been published in which it was shown that the regridding method is an approximation to the least-squares solution [40]. Moreover, a framework for the calculation of the optimal gridding parameters was given. This framework has only been validated by a hardware phantom study. Our results, including the in vivo images obtained with a spiral trajectory, are in agreement with the conclusion that the regridding method offers an approximation to the least-squares approach.

Some remarks concerning the reconstruction time are in order. Solving the eigenvalue problem that is related to the MNLS reconstruction method is a time-consuming step. It took about 75 minutes (in double precision) on a Digital Personal Workstation (500 au, 704-Mb RAM) for the case of M =4033 different data points. The calculation of the pseudoinverse $(\mathcal{H}\mathcal{H}^{\dagger})^{+}$ from the solution of the eigenvalue problem took

about 30 min. It should be emphasized, however, that the eigenvalue-problem and $(\mathcal{H}\mathcal{H}^{\dagger})^{+}$ pseudoinverse calculations must be performed only once for each data grid (i.e., for each type of data acquisition). The calculation of the MNLS image from the knowledge of the pseudoinverse and the MR data requires a number of multiplications in the order of M^2, and the reconstruction of an MNLS image from the knowledge of the pseudoinverse and the MR data took only a few seconds.

As was stated before, in the case of MNLS image reconstruction, discretization in the image domain is performed only after the actual image reconstruction. The proposed MNLS image reconstruction results in a *continuous* image function, which is not the case for existing reconstruction schemes such as discrete Fourier transform, FBP, or regridding. As a result, MNLS image reconstruction would allow us to visualize images on a random grid in the image domain directly, i.e., without interpolation. Moreover, the choice of the image grid has no influence on the image reconstruction and can be chosen arbitrarily.

V. Conclusion

In this paper, an MNLS image-reconstruction method was presented, which is based on a general formalism for CD mapping and pseudoinverse calculation. The method is an alternative to existing regridding-based image reconstruction methods when MR data are sampled on a non-Cartesian grid. The fact that the method results in a continuous image function, and the fact that it does not involve any regridding or interpolation of the acquired data makes it fundamentally different from existing image-reconstruction methods.

The potential of the method was illustrated by simulations and in vivo experiments. Two data-acquisition techniques were considered: radial and spiral imaging. Simulations based on radial sampling showed the importance of a careful choice of a singular-value threshold during the reconstruction of images based on the formalism that was proposed in this paper. This is due to the ill-conditionedness of the problem. In the case of spiral imaging, simulations revealed that MNLS image reconstruction can result in a drastic decrease of artifacts compared with the widely used regridding-based reconstruction that was presented earlier by Jackson [24]. Also in experiments with spiral MRI, a decrease of artifacts in the case of MNLS image reconstruction was observed, as well as an increase of both SNR and image contrast.

A recent study has been reporting promising results concerning an improved regridding method compared to Jackson's method [40]. A comparison of our results to the results that are obtained by this method could be an interesting topic for future research. Moreover, a task-based assessment of the proposed reconstruction method could be a next topic of research. When high resolution is primordial, the slightly lower spatial resolution in MNLS images could be a drawback of the method. However, applications were the SNR is important (e.g., detection of low-contrast lesions or low-contrast image changes) could benefit from the MNLS image reconstruction approach.

Appendix
Analytical Expression for the Raw Data of the Shepp and Logan Head Phantom

The SL head phantom is the superposition of several ellipses in the image domain. Therefore, the corresponding raw data can be calculated analytically once an analytical expression for the FT of a general ellipse is known. This expression will be derived in this appendix.

An ellipse that is centered at the origin (i.e., its center point $(x_1, y_1) = (0, 0)$) and has axes parallel to the x and y axes, can be described by

$$e_0(\overline{r}) = \begin{cases} \rho, & \text{if } \dfrac{x^2}{A^2} + \dfrac{y^2}{B^2} \leq 1 \\ 0, & \text{otherwise} \end{cases} \tag{18}$$

with (x, y) being the coordinates that correspond to the position vector $\overline{r}$, A and B are the axes of the ellipse, and ρ is its intensity. The continuous 2-D MR raw-data function that corresponds to the ellipse, $e_0(\overline{r})$, equals its FT. By using the Fourier slice theorem [42], and by considering Poisson's Bessel function formula [43], the MR signal corresponding to the projection of $e_0(\overline{r})$ along a projection axis with projection angle θ can be written in polar (k, θ)-coordinates

$$S_{0,\theta}(k) = \rho AB \frac{J_1(2\pi a_0(\theta)k)}{a_0(\theta)k} \tag{19}$$

with $a_0(\theta) = \sqrt{A^2\cos^2(\theta) + B^2\sin^2(\theta)}$ and $J_1(\cdot)$ denoting the first-order Bessel function of the first kind.

Now we consider a general ellipse $e(\overline{r})$, i.e., an ellipse with arbitrary center point (x_1, y_1) and rotation angle α relative to the x-axis. The projections $P_\theta(r)$ of $e(\overline{r})$ are related to the projections $P_{0,\theta}(r)$ of $e_0(\overline{r})$ by

$$P_\theta(r) = P_{0,\theta-\alpha}(r - t\cos(\gamma - \theta)) \tag{20}$$

with $t = \sqrt{x_1^2 + y_1^2}$ and $\gamma = \arctan(y_1/x_1)$. By using equations (19) and (20) on the one hand and the Fourier shift theorem on the other hand [42], we finally obtain an analytical expression for the MR signal $S_\theta(k)$ that corresponds to $e(\overline{r})$

$$S_\theta(k) = \exp\left[-j2\pi kt\cos(\gamma - \theta)\right] \rho AB \frac{J_1(2\pi a(\theta)k)}{a(\theta)k} \tag{21}$$

with $a(\theta) = \sqrt{A^2\cos^2(\theta - \alpha) + B^2\sin^2(\theta - \alpha)}$.

Acknowledgment

The authors thank Dr. G. H. Glover from Stanford University, Stanford, CA. for providing the spiral imaging sequence and regridding software that was used in this study, and Dr. T. P. Trouard from the University of Arizona, Tucson, AZ, for helpful discussions. R. Van de Walle is Post-Doctoral Fellow of the Fund for Scientific Research, Flanders (FWO, Belgium).

References

[1] W. H. Press, B. P. Flannery, S. A. Teukolsky, and W. T. Vetterling, *Numerical Recipes in C: The Art of Scientific Computing*. Cambridge, U.K.: Cambridge Univ. Press, 1997.

[2] E. O. Brigham, *The Fast Fourier Transform and Applications*. Englewood Cliffs, NJ: Prentice-Hall, 1988.
[3] M. Hedley, H. Yan, and D. Rosenfeld, "Motion artifact correction in MRI using generalized projections," *IEEE Trans. Med. Imag.*, vol. 10, pp. 40–46, Feb. 1991.
[4] G. H. Glover and J. M. Pauly, "Projection reconstruction techniques for reduction of motion effects in MRI," *Magn. Reson. Med.*, vol. 28, pp. 275–289, 1992.
[5] A. F. Gmitro and A. L. Alexander, "Use of a projection reconstruction method to decrease motion sensitivity in diffusion-weighted MRI," *Magn. Reson. Med.*, vol. 29, pp. 835–838, 1993.
[6] R. Van de Walle, T. Voet, and I. Lemahieu, "The motion sensitivity of magnetic resonance imaging: A comparison between Fourier transform imaging and projection reconstruction," in *Proc. IEEE EMBC and CMBEC, 17th Conf.*, Montreal, PQ, Canada, 1995, pp. 457–458.
[7] R. Van de Walle, I. Lemahieu, J. Peynsaert, Y. De Deene, and E. Achten, "Motion detection from the measured signals in magnetic resonance imaging," *Signal Processing*, vol. 55, pp. 375–379, 1996.
[8] R. Van de Walle, I. Lemahieu, and E. Achten, "Two motion-detection algorithms for projection-reconstruction magnetic resonance imaging: Theory and experimental verification," *Comput. Med. Imag. Graph.*, vol. 22, pp. 115–121, 1998.
[9] A. T. Lee and G. H. Glover, "Motion artifacts in fMRI: Comparison of 2DFT with PR and spiral scan methods," *Magn. Reson. Med.*, vol. 33, pp. 624–635, 1995.
[10] M. L. Lauzon and B. K. Rutt, "Effects of polar sampling in k-space," *Magn. Reson. Med.*, vol. 36, pp. 940–949, 1996.
[11] D. C. Peters, C. A. Mistretta, F. R. Korosec, J. Holden, F. Kelcz, K. Wedding, and T. Grist, "Using projection reconstruction with a limited number of projections to increase image resolution or acquisition speed," in *Proc. ISMRM 6th Scientific Meeting*, Sydney, Australia, 1998, p. 182.
[12] P. Mansfield, "Multi-planar image formation using NMR spin echoes," *J. Phys. C.*, vol. 10, pp. L55–L58, 1977.
[13] C. B. Ahn, J. H. Kim, and Z. H. Cho, "High-speed spiral-scan echo planar NMR imaging," *IEEE Trans. Med. Imag.*, vol. MI-5, pp. 2–7, Feb. 1986.
[14] C. H. Meyer, B. S. Hu, D. G. Nishimura, and A. Macovski, "Fast spiral coronary artery imaging," *Magn. Reson. Med.*, vol. 28, pp. 202–213, 1992.
[15] D. C. Noll, J.D. Cohen, C. H. Meyer, and W. Schneider, "Spiral k-space MR imaging of cortical activation," *J. Magn. Reson. Imag.*, vol. 5, pp. 49–56, 1995.
[16] T. B. Harshbarger and D. B. Twieg, "Iterative reconstruction of single-shot spiral MRI with off resonance," *IEEE Trans. Med. Imag.*, vol. 18, pp. 196–205, Mar. 1999.
[17] D. C. Noll, "Multi-shot rosette trajectories for spectrally selective MR imaging," *IEEE Trans. Med. Imag.*, vol. 16, pp. 372–377, 1997.
[18] D. C. Noll, "Simultaneous multislice acquisition using rosette trajectories (SMART): A new imaging method for functional MRI," *Magn. Reson. Med.*, vol. 39, pp. 709–716, 1998.
[19] K. Scheffler and J. Hennig, "Frequency resolved single-shot MR imaging using stochastic k-space trajectories," *Magn. Reson. Med.*, vol. 35, pp. 569–576, 1996.
[20] G. T. Herman, *Image Reconstruction From Projections, Implementations and Applications*. Berlin, Germany: Springer Verlag, 1979.
[21] P. G. Morris, *Nuclear Magnetic Resonance Imaging in Medicine and Biology*. New York: Oxford Univ. Press, 1986.
[22] Z. H. Cho, J. P. Jones, and M. Singh, *Foundations of Medical Imaging*. New York: Wiley, 1993.
[23] J. O'Sullivan, "A fast sinc function gridding algorithm for Fourier inversion in computer tomography," *IEEE Trans. Med. Imag.*, vol. MI-4, pp. 200–207, 1985.
[24] J. I. Jackson, C. H. Meyer, D. G. Nishimura, and A. Macovski, "Selection of a convolution function for Fourier inversion using gridding," *IEEE Trans. Med. Imag.*, vol. 10, pp. 472–478, 1991.
[25] D. Rosenfeld, "An optimal and efficient new gridding algorithm using singular value decomposition," *Magn. Reson. Med.*, vol. 40, pp. 14–23, 1998.
[26] L. Axel, G. T. Herman, D. A. Roberts, and L. Dougherty, "Linogram reconstruction for magnetic resonance imaging MRI," *IEEE Trans. Med. Imag.*, vol. 9, pp. 447–449, 1990.
[27] M. Bertero, C. De Mol, and E. Pike, "Linear inverse problems with discrete data. I: General formulation and singular system analysis," *Inverse Problems*, vol. 1, pp. 301–330, 1985.
[28] M. Bertero, C. De Mol, and E. Pike, "Linear inverse problems with discrete data: II. Stability and regularization," *Inverse Problems*, vol. 4, pp. 573–594, 1988.
[29] G. T. Gullberg, Y. L. Hsieh, and G. L. Zeng, "An SVD reconstruction algorithm using a natural pixel representation of the attenuated radon transform," *IEEE Trans. Nucl. Sci.*, vol. 43, pp. 295–303, 1996.
[30] M. H. Buonocore, W. R. Brody, and A. Macovski, "A natural pixel decomposition for two-dimensional image reconstruction," *IEEE Trans. Biomed. Eng.*, vol. BME-28, pp. 69–78, 1981.
[31] F. Natterer, *The Mathematics of Computerized Tomography*. New York: Wiley, 1989.
[32] A. Rosenfeld and A. Kak, *Digital Picture Processing*. New York: Academic, 1982.
[33] Y. M. Kadah and X. Hu, "Algebraic reconstruction for magnetic resonance imaging under B0 inhomogeneity," *IEEE Trans. Med. Imag.*, vol. 17, pp. 362–370, 1998.
[34] G. Sansone, *Orthogonal Functions*. New York: Dover, 1991.
[35] A. Messiah, *Quantum Mechanics I*. Amsterdam, The Netherlands: North-Holland, 1961.
[36] R. Penrose, "A generalized inverse for matrices," in *Proc. Cambridge Phil. Soc.*, vol. 51, 1955, pp. 406–413.
[37] C. L. Lawson and R. J. Hanson, *Solving Least Squares Problems*. Philadelphia, PA: Soc. Ind. Appl. Math., 1995.
[38] Linear algebra PACKage, basic linear algebra subprograms. [Online]. Available: http://www.netlib.org/lapack/index.html
[39] S. R. Deans, *The Radon Transform and Some of Its Applications*. New York: Wiley, 1983.
[40] H. Searat and D. Nishimura, "On the optimality of the gridding reconstruction algorithm," *IEEE Trans. Med. Imag.*, vol. 19, pp. 306–317, Apr. 2000.
[41] A. V. Thikonov and V. Y. Arsenin, *Solution of Ill-Posed Problems*: Winston and Sons, 1977.
[42] N. Morrison, *Introduction to Fourier Analysis*. New York: Wiley, 1994.
[43] S. Iyanaga and Y. Kawada, *Encyclopedic Dictionnary of Mathematics*. Cambridge, MA: MIT Press, 1980.